# 2. POINT-SOURCE/POINT-RECEIVER METHODS

A. G. Every
Department of Physics
University of the Witwatersrand
Johannesburg, South Africa

K. Y. Kim and W. Sachse
Department of Theoretical and Applied Mechanics
Cornell University
Ithaca, New York

## 2.1 Introduction

This chapter deals with a suite of techniques that elicit information on the elastic properties of solids using pointlike excitation and detection of ultrasound. These point-source/point-receiver (PS/PR) techniques have shown great promise in several materials' inspection and characterization applications. One of their advantages is that a point source generates both longitudinal and shear waves in a specimen, and therefore information about both types of waves can, in principle, be extracted from a single waveform. Furthermore, PS/PR signals are simultaneously propagated in a wide range of directions in a specimen, and so one can use an array of sensors or scan either the source or the receiver over the specimen surface to determine the directional dependence of the speeds of propagation and amplitudes of various wave modes in a material. When a repetitive source is used, a number of signals measured at adjacent source–receiver configurations can be stacked together to obtain a so-called *scan image*, which portrays the detailed spatial and temporal characteristics of the elastic wavefield in a material, and this can be directly related to the material's anisotropy and macrostructure [1]. Although PS/PR techniques offer the advantage of simplicity in sample preparation and data collection, there is a trade-off, and that is added complexity in extracting information about the sample from the wavefield data.

The term PS/PR usually attaches to a technique that delivers acoustic energy to a region comparable in size to, or smaller than, the characteristic wavelength radiated, and to detection of the wavefield within a similarly small area. Incoherent excitation over a larger region, as occurs in phonon imaging [2, 3], can be categorized as PS/PR, provided that the coherence length is sufficiently



EXPERIMENTAL METHODS IN THE PHYSICAL SCIENCES
Vol. 39
ISBN 0-12-475986-6



ISSN 1079-4042/01 $35.00

small and the observation distance is much greater than the source size. An essential characteristic of point excitation is that, instead of waves of a single wave normal being excited, as is the case with conventional pulse-echo techniques, the waveform is a superposition of waves with a broad spread of wave normals. Radiation of acoustic energy consequently takes place in a wide range of directions, and detection has similar wide-angle sensitivity. These techniques, in essence, measure a time or frequency domain dynamic Green's function (response function) of the solid. As such, PS/PR techniques explore phenomena that are not normally encountered in plane wave techniques. For an impulsive or suddenly applied force, the response displays a number of wave arrival singularities, which propagate outwards from the source at group velocity in each direction. Periodic excitation reveals internal diffraction effects. In the far field, the wave arrival rays and associated acoustic energy focusing dominate the observations. Transient techniques can be considered simulated acoustic emission [4]; they produce similar waveforms to actual acoustic emission or seismic events, but in a more controlled way.

There are a number of techniques available for performing PS/PR measurements. The fracture of a very small capillary [5, 6] or pencil lead [7] on the surface of a sample simulates a point force acting normal to the surface and having a step function time dependence. A focused pulsed laser beam of sufficient energy to cause ablation of a specimen's surface simulates a point impulse normal to that surface, and a horizontal double force is realized when the pulsed laser beam operates in the thermoelastic regime [8–10]. Much the same effect can be achieved with electron beams [11] and x-rays [12]. Pointlike detection can be achieved, for example, with piezoelectric "pinducers," with small capacitive detectors [6], or by laser interferometry [13–15]. Focusing an acoustic beam through a transmission fluid onto a surface allows pulsed or periodic forces to be generated and surface displacements to be detected [16–20]. Optical techniques for excitation and detection have the advantage of being noncontact. Discussion of the comparative operational characteristics of a number of sources and receivers that can be used in PS/PR measurements can be found in [21].

To date, ultrasonic PS/PR measurements of elastic constants have been carried out on a number of crystals (see, e.g., [22–31]) and also on a variety of polymer and ceramic–ceramic matrix composite specimens (see, e.g., [32–35]). In the case of composites, signals possessing excellent signal-to-noise ratio are detected even when the materials exhibit high damping characteristics that make conventional ultrasonic measurements difficult or even impossible.

## 2.2 Dynamic Green's Functions: Formal Solutions

The phenomena we describe in this chapter, as mentioned earlier, can be interpreted directly or indirectly in terms of dynamic Green's functions. Some

of these phenomena are reasonably well accounted for by the Green's functions for an infinite anisotropic elastic continuum [36–38], whereas for others the surfaces play a vital role. Where necessary we will be treating the effects of surfaces either in an ad hoc matter, or invoke the dynamic Green's function for a half-space [39–42] in the interpretation. Our concluding discussion is on transient waves in thin anisotropic plates.

### 2.2.1 Infinite Continuum Green's Functions

The space-time response or Green's function $G_{ij}(\mathbf{x}, t)$ for an infinite anisotropic elastic continuum is governed by the equation

$$\left(\rho\delta_{mi}\frac{\partial^2}{\partial t^2} - c_{mki\ell}\frac{\partial^2}{\partial x_k \partial x_\ell}\right) G_{ij}(\mathbf{x}, t) = \delta_{mj}\delta(\mathbf{x})F(t) \tag{2.1}$$

Physically $G_{ij}(\mathbf{x}, t)$ represents the $i$'th Cartesian component of the displacement at point $\mathbf{x}$ and time $t$ in response to a concentrated force in the $j$'th direction having time dependence $F(t)$, applied at the origin. The array of responses $G_{ij}(\mathbf{x}, t)$, $i, j = 1, 2, 3$, form a tensor of second rank. The formal solution to Eq. 2.1 in terms of integral transforms has been treated by a number of authors [36–38, 43–47], and the methods have been reviewed by Payton [48]. In brief, by carrying out a quadruple space-time Fourier transform on Eq. 2.1, solving the resultant algebraic equations, and then carrying out the inverse transform, one obtains

$$G_{ij}(\mathbf{x}, t) = \int G_{ij}(\mathbf{x}, \omega) f(\omega) e^{-i\omega t}\, d\omega \tag{2.2}$$

where

$$G_{ij}(\mathbf{x}, \omega) = \frac{1}{(2\pi)^3}\int d^3\mathbf{k}(L^{-1}(\mathbf{k}, \omega))_{ij} e^{i\mathbf{k}.\mathbf{x}} \tag{2.3}$$

$$L_{mi}(\mathbf{k}, \omega) = c_{mki\ell}k_k k_\ell - \rho\omega^2\delta_{mi} \tag{2.4}$$

and

$$f(\omega) = \frac{1}{2\pi}\int F(t)\, e^{i\omega t}\, dt \tag{2.5}$$

is the Fourier transform of the forcing function. Using the spectral resolution theorem [49], we can write

$$(L^{-1})_{ij} = \sum_{n=1}^{3} \frac{\Lambda_{ij}^{(n)}}{\rho v^{(n)2}k^2 - \rho\omega^2} = \sum_{n=1}^{3} \frac{s^{(n)2}\Lambda_{ij}^{(n)}}{\rho(k^2 - \omega^2 s^{(n)2})} \tag{2.6}$$

where the sum is taken over the three eigensolutions of the Christoffel tensor $\Gamma_{mi} = c_{mki\ell} n_k n_\ell$, and $v^{(n)}$ is the phase velocity, $s^{(n)} = 1/v^{(n)}$ the slowness, $\Lambda_{ij}^{(n)} = U_i^{(n)} U_j^{(n)}$, and $\mathbf{U}^{(n)}$ is the polarization vector for each mode. The integral over the magnitude of $\mathbf{k}$ can be done analytically [36, 37], leading to the equation

$$G_{ij}(\mathbf{x}, \omega) = \frac{1}{8\pi^2 \rho} \sum_n \left\{ i\omega \int_\cap d\Omega s^{(n)3} \Lambda_{ij}^{(n)} e^{i\omega \mathbf{s}^{(n)}.\mathbf{x}} + \frac{1}{x} \int_0^{2\pi} d\phi s^{(n)2} \Lambda_{ij}^{(n)} \right\} \tag{2.7}$$

for the frequency domain Green's function $G_{ij}(\mathbf{x}, \omega)$. The first of the two integrals is with respect to the direction of the slowness $\mathbf{s} = \mathbf{k}/\omega$, and is carried out over the unit hemisphere centered on the observation direction, with $d\Omega$ denoting the element of solid angle in which $\mathbf{s}$ falls. The second integral is a line integral taken around the periphery of this hemisphere.

We evaluate $G_{ij}(\mathbf{x}, t)$ for a point force with step function time dependence

$$F(t) = \Theta(t) = \begin{cases} 0, & t < 0 \\ 1, & t > 0 \end{cases} \tag{2.8}$$

The Fourier transform of $\Theta(t)$ is $f(\omega) = -1/2\pi i\omega + \delta(\omega)/2$, and from Eq. 2.2 it follows that

$$G_{ij}(\mathbf{x}, t) = \frac{1}{8\pi^2 \rho} \sum_n \left\{ -\int_\cap d\Omega s^{(n)3} \Lambda_{ij}^{(n)} \delta(t - \mathbf{s}.\mathbf{x}) + \frac{\Theta(t)}{x} \int_0^{2\pi} d\phi s^{(n)2} \Lambda_{ij}^{(n)} \right\}. \tag{2.9}$$

The response to an impulsive force $F(t) = \delta(t)$ is the time derivative of $G_{ij}(\mathbf{x}, t)$, and the response to other force distributions and time dependences can be obtained by integration.

### 2.2.2 Half-space Green's Functions

We take the Fourier domain surface Green's function for an anisotropic solid as our starting point for calculating the transient response of a half-space, following the method of Every *et al.* [39]. Generalizing to an arbitrary component of surface force, and to the response at an interior point of an anisotropic elastic half-space ($hs$) at a distance $x_3$ from the surface, we have

$$G_{ij}^{hs}(\mathbf{k}_\parallel, x_3, \omega) = \frac{i}{\omega} \sum_{n=1}^{3} E_{ij}^{(n)} \exp\{ik_3^{(n)} x_3\} \tag{2.10}$$

$$E_{ij}^{(n)}(\mathbf{s}_\parallel) = \frac{\text{adj}(\mathbf{B})_j^{(n)} U_i^{(n)}}{\det |\mathbf{B}|} \tag{2.11}$$

and $\mathbf{s}_\parallel = \mathbf{k}_\parallel/\omega$. By Fourier transforming with respect to $\mathbf{k}_\parallel$ and $\omega$, and replacing the integration variable $\mathbf{k}_\parallel$ by $\mathbf{s}_\parallel$, we arrive at the following integral expression:

$$G_{ij}^{hs}(\mathbf{x}, t) = -\frac{1}{4\pi^3}\int_{-\infty}^{\infty} d^2 s_\parallel \int_0^{\infty} d\omega \sum_{n=1}^{3} E_{ij}^{(n)} \exp\{i\omega(\mathbf{s}_\parallel.\mathbf{x}_\parallel + s_3^{(n)} x_3 - t)\} + I \tag{2.12}$$

for the response of the medium to a concentrated point force acting on the surface and having step function time dependence $\Theta(t)$. $I$ is an integration constant. Without loss of generality, we can choose the observation point to be in the $(x_1, x_3)$ plane, setting $x_2 = 0$. The integration over $\omega$ can be done analytically to yield

$$G_{ij}^{hs}(\mathbf{x}, t) = -\frac{1}{4\pi^3|\mathbf{x}|} Re \int_{-\infty}^{\infty} d^2 s_\parallel \sum_{n=1}^{3} \frac{i E_{ij}^{(n)}(\mathbf{s}_\parallel)}{s_1 \sin\theta + s_3^{(n)} \cos\theta - t/|\mathbf{x}| + i0_+} + I \tag{2.13}$$

For the surface response ($x_3 = 0$) we can use causality to simplify further, finally obtaining

$$G_{ij}^{hs}(x_1, t > 0) = -\frac{1}{2\pi^2|x_1|} Re\{\Phi_{ij}(t/x_1) - \Phi_{ij}(0)\} \tag{2.14}$$

where

$$\Phi_{ij}(s_1) = \int_{-\infty}^{\infty} ds_2 \sum_{n=1}^{3} E_{ij}^{(n)}(s_1, s_2) \tag{2.15}$$

Calculated responses are presented later.

## 2.3 Response to a Periodic Force: Numerical Implementation and Comparison with Experiment

For an isotropic solid the angular integrals in Eq. 2.7 for the infinite continuum response function $G_{ij}(\mathbf{x}, \omega)$ can be performed analytically [4], but for anisotropic solids, except in certain special cases [48], these integrals require numerical methods for their evaluation. The first term in Eq. 2.7, because it involves 2D integration, is the most computationally demanding. The main reason for this is the rapid variation of the phase factor, which necessitates a fine grid size for the integration. Of interest to us here is the far field $\omega s x > 200\pi$ and the intermediate field $200\pi > \omega s x > 2\pi$.

### 2.3.1 The Far Field

For the far field we invoke the stationary phase approximation and limit the integration to small regions around directions in which the phase $\omega\mathbf{s}.\mathbf{x}$ is

stationary. The contribution from all other directions is negligible because of the rapid phase variation of the integrand and resulting cancellation. At the stationary phase points, the outward normal to the slowness surface, which is the direction of the group velocity $\mathbf{V}$ is parallel to the observation direction $\mathbf{x}$. Thus, to obtain the response at a point requires identifying the group velocities in that direction.

There are various methods for calculating the group velocity $\mathbf{V} = \nabla_{\mathbf{k}}\omega(\mathbf{k})$ for a wave, all of which involve expressing it parametrically in terms of quantities that are derivable from Christoffel's equation. The more frequently encountered are the following [50–52]. Differentiating Christoffel's equation yields

$$V_i = \frac{1}{\rho v} c_{ijkl} n_k U_j U_l \tag{2.16}$$

$\mathbf{V}$ can also be obtained from the phase velocity equation by implicit differentiation. Arranging this equation to be homogeneous in the components of $\mathbf{n}$, one has

$$\mathbf{V} = \frac{\partial v}{\partial \mathbf{n}} \tag{2.17}$$

The fact that the group velocity is normal to the constant frequency and slowness surfaces leads to two other expressions for $\mathbf{V}$:

$$\mathbf{V} = -\frac{\nabla_{\mathbf{k}} D(\mathbf{k}, \omega)}{\partial D/\partial \omega} = \frac{\nabla_{\mathbf{s}} S(\mathbf{s})}{\mathbf{s} \cdot \nabla_{\mathbf{s}} S(\mathbf{s})} \tag{2.18}$$

where the dispersion relation $D(\mathbf{k}, \omega) = 0$ and the slowness equation $S(\mathbf{s}) = 0$.

In these small regions around the stationary phase points, the factor $s^3\Lambda$ can be taken to be constant, and for a generic point the equation for the slowness surface can be approximated by $s_3 = L_1 s_1^2 + L_2 s_2^2$ in a locally oriented coordinate system with $s_3$ normal to the surface and $s_1$ and $s_2$ along the directions of the principal curvatures of the surface. $L_1$ and $L_2$ are the values of these principal curvatures, and their product, $K = L_1 L_2$, is the Gaussian curvature of the surface. The integral can now be performed analytically, yielding a contribution to $G_{ij}(\mathbf{x}, \omega)$ of the form [37, 44]

$$G \approx \frac{s\Lambda e^{i\omega \mathbf{s}.\mathbf{x}}}{\rho x \sqrt{|L_1 L_2|}} \tag{2.19}$$

for each stationary phase point. The intensity or energy flux $I$ associated with each contribution is proportional to $|G|^2$, and thus

$$I \approx \frac{1}{x|K|} \tag{2.20}$$

We will see that this result has a simple geometrical interpretation on the basis of ray acoustics, and that the variation of $K$ in an anisotropic solid can have striking consequences.

### 2.3.2 Phonon Imaging

The acoustic anisotropy of crystals is revealed in a most graphic way in phonon imaging [2]. In this technique a focused laser or electron beam is used to heat a small spot on the surface of a single crystal specimen maintained at an ambient temperature of $\approx$2K. The thermal phonons emanating from this heated region (they can be thought of as small wave packets with frequencies in the region of 100 GHz) travel ballistically through the crystal to the opposite face, where they are detected with a superconducting bolometer or tunnel junction detector. A phonon image depicts the directional dependence of the transmitted phonon intensity and is constructed by raster-scanning the source over the front surface and recording the detected signal as a gray-scale image. Figure 2.1(a) shows a measured phonon image for the crystal sapphire ($Al_2O_3$) [53], time-gated to display only the ST and FT phonon flux. The phonon intensity is highly nonuniform, mainly ascribable to the effect of phonon focusing discussed in the following text. The bright lines are caustics, where the flux is mathematically singular.

Phonon focusing has its origin in the nonspherical shape of the acoustic slowness surface. The rays pointing out of this surface can be taken to represent the group velocity vectors of the phonons making up the heat flux. It is evident that, where the curvature of the slowness surface is least, the group velocity vectors are strongly concentrated in direction, and consequently the energy flux in that direction is the greatest. This effect is known as phonon focusing, and it is the most important source of nonuniformity of the intensity in phonon images. A useful measure of focusing is given by the Maris phonon enhancement factor [3, 54]

$$A = \left| \frac{\delta\Omega_{\mathbf{s}}}{\delta\Omega_{\mathbf{V}}} \right| \tag{2.21}$$

where $\delta\Omega_{\mathbf{s}}$ is the solid angle subtended by an infinitesimal cone of slowness vectors and $\delta\Omega_{\mathbf{V}}$ is the solid angle subtended by their associated group velocity vectors. From differential geometry it is readily established that [55, 56]

$$A = (s^3 V |K|)^{-1} \tag{2.22}$$

This geometrical argument thus leads to the same conclusion as the stationary phase approximation for the far field, namely, that the energy flux in any direction for a particular mode is inversely proportional to the magnitude of the Gaussian curvature, $|K|$, of the slowness surface.

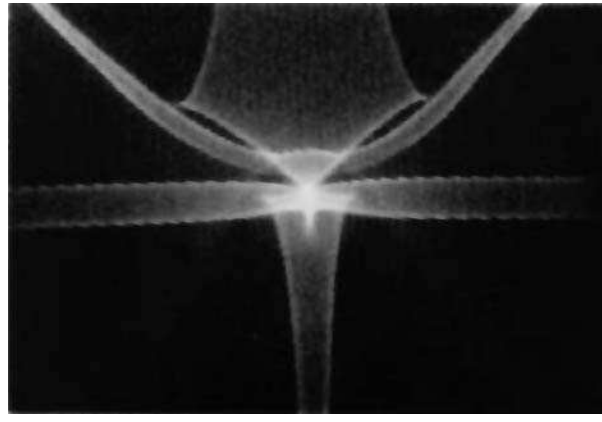

(a)

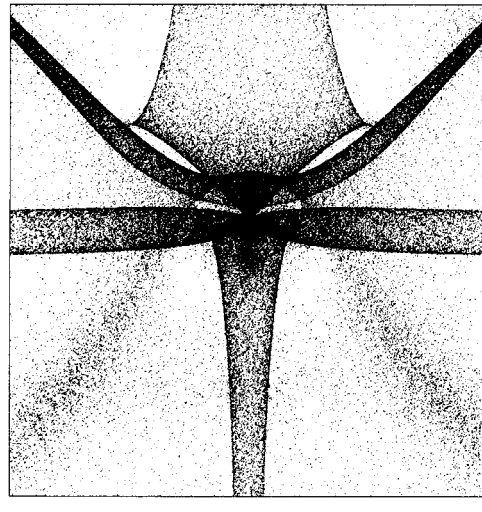

(b)

FIG. 2.1. (a) Measured phonon image for the crystal sapphire ($Al_2O_3$), time-gated to display only the ST and FT phonon flux. Bright regions indicate directions of high phonon intensity. (b) Monte Carlo calculated focusing pattern for sapphire (darkness in this case is a measure of the phonon intensity).

Monte Carlo methods provide the simplest means of generating theoretical phonon intensity patterns of crystals [2]. A common point of departure in these computer simulations is to assume that the phonons emanating from the heat source have a uniform distribution of wave normals. The group velocities for a large number of uniformly distributed normals are computed, and the points

where these meet the viewing surface are sorted into a two-dimensional array of bins, and the result presented as a gray-scale image. Figure 2.1(b) shows the calculated focusing pattern for sapphire for the experimental geometry of Figure 2.1(a). The values of the elastic constants in this calculation have been adjusted to obtain the best fit to experiment. Actually, it is only the elastic constant ratios that can be determined in this way, since changing all the elastic constants by the same factor does not alter a phonon focusing pattern. The values of the elastic constants obtained are close to the low-temperature extrapolated values used in [53]. Interestingly, the fit is most sensitive to the value of $C_{14}$, an elastic constant that is not normally easy to measure accurately (the fitted value is $-23.2 \pm 0.3$ GPa). Metzger and Huebener [57] have made similar adjustments to the values of the elastic constants in fitting calculated to measured phonon image of germanium. Their fitted values differ appreciably from literature values, and they conclude that this is the result of dispersion.

The most striking feature of the phonon images in Figure 2.1 is the complex pattern of caustics they contain. These intense bands are associated with lines of zero Gaussian curvature on the slowness surface [55]. The vanishing of $K$ on these lines results in the energy flux being mathematically infinite. Caustics are essentially a far-field effect. The patterns they form for different crystal symmetries and degrees of anisotropy have been extensively studied by a number of authors. For a review, see [2].

### 2.3.3 Intermediate Field

Emerging from the far field, as the frequency is lowered or the observation point is brought closer to the source, each line caustic of a phonon focusing pattern unfolds into an Airy diffraction pattern [58, 59]. As the frequency is lowered further, the fringes broaden and merge, becoming fewer in number. To predict the diffraction pattern requires going beyond the stationary phase approximation and carrying out the numerical integration in Eq. 2.7. In the intermediate field the main contributions to the integral still come from the vicinity of stationary phase points, and one can, without much loss of accuracy, still restrict the integration to small but finite regions around each such point.

### 2.3.4 Scanning Transmission Acoustic Microscopy

Scanning transmission acoustic microscopy has been used by Hauser *et al*. [18] to study the frequency domain dynamic response of a number of anisotropic solids, including metal, insulating and semiconducting crystals, and fiber composites. Their experimental setup is shown in Figure 2.2(a). A pair of water immersion acoustic lenses, which are focused to small spots on opposite surfaces of the sample, are used to generate and detect ultrasonic tone bursts with central frequencies in the range of 5 to 25 MHz. One of the transducers

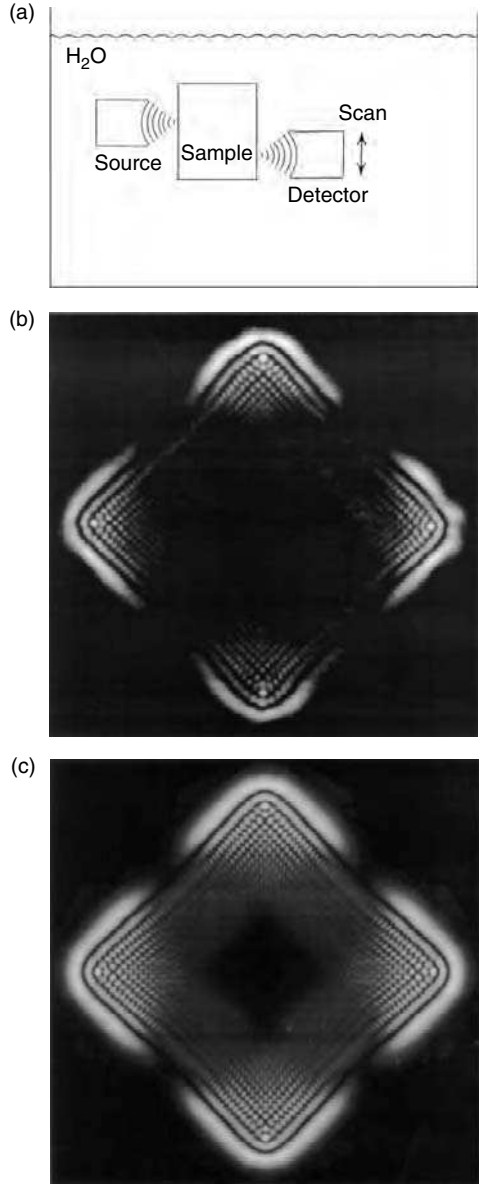


FIG. 2.2. (a) Experimental scanning transmission acoustic microscopy technique of Hauser *et al*. [18]. (b) Internal diffraction image of GaAs centered on the [100] direction, measured by Wuerz *et al*. [27, 28], (c) Their calculated image, based on optimized values of the elastic constants.

TABLE 2.1. Elastic Constants of GaAs

| | $C_{11}(GPa)$ | $C_{12}(GPa)$ | $C_{44}(GPa)$ |
|---|---|---|---|
| Wuerz *et al.* [27] | 118.52 | 54.99 | 57.77 |
| Tabulated values [60] | 118 | 53.5 | 59.4 |

is kept fixed while the other is raster-scanned to yield a two-dimensional image of the ultrasonic flux pattern transmitted through the sample. The measured diffraction images are in good agreement with calculated Green's functions $G_{33}(\mathbf{x}, \omega)$ corresponding to the experimental parameters. The actual analysis carried out by Hauser *et al.* [18] is a little different from this, in that they also take account of the finite angular width of the incoming and outgoing beams in the water and of the angular dependence of the transmission across the fluid–solid interface. Wesner *et al.* [19] have used essentially the same technique to study a number of crystals, except that they retain phase information and operate at higher frequencies. Kim *et al.* [36] have studied the diffraction of SH waves in Si using piezoelectric shear transducers.

2.3.4.1 Recovery of Elastic Constants from Diffraction Images. Wuerz *et al.* [27, 28] have determined the elastic constants of GaAs by fitting a calculated diffraction image to measurement for that crystal. Figure 2.2(b) shows their measured image. They have used a simplex inversion algorithm to obtain the elastic constants, starting from remote values. Figure 2.2(c) is the best fit to their early time image, and the Table 2.1 shows the elastic constant values they obtain from this fit, which are in close agreement with tabulated values. In contrast to phonon imaging, all the elastic constants are obtained from a diffraction image, not simply the ratios. This is because the magnitudes of the elastic constants determine the fringe spacing. Interestingly, in their fit Wuerz *et al.* [27] use only information pertaining to the ST branch extending out to about 13° from the [100] direction, and yet are able to accurately recover all three of the elastic constants of GaAs. It is unlikely that one would be able to achieve the same accuracy with ST phase velocity measurements in the same angular range. The algorithm of Wuerz *et al.* [27] appears to be quite robust, although CPU intensive.

## 2.4 Time Domain Response: Numerical Implementation and Comparison with Experiment

### 2.4.1 Infinite Continuum Response

To evaluate $G_{ij}(\mathbf{x}, t)$ at a particular time, the first term in Eq. 2.9 can be reduced to a one-dimensional integral summed over directions for which

$t - \mathbf{s}.\mathbf{x} = 0$. However, it is usual that the entire time dependence of $G_{ij}(\mathbf{x}, t)$ is required, in which case it is simpler, and not necessarily more demanding on computer time, to perform the two-dimensional integration as a sorting and counting process. The time interval between $t = 0$ and the arrival of the last wave, i.e., the largest value of $\mathbf{s}.\mathbf{x}$, is divided into a number of slots. A uniform distribution of $\mathbf{n}$'s is generated, and for each of these the value of $\mathbf{s}.\mathbf{x}$ determines the slot in which the corresponding value of $s^3\Lambda_{ij}$ is accumulated. For times exceeding the maximum of $\mathbf{s}.\mathbf{x}$, $G_{ij}(\mathbf{x}, t)$ has the constant value given by the second term in Eq. 2.9. By way of example, Figure 2.3(a) shows calculated infinite continuum responses $G_{33}(\mathbf{x}, t)$ for hexagonal zinc ($x_3$ axis taken along the principal crystallographic axis) [39] for three observation points, namely, $x_1 = 0$ mm, 5 mm, and 10 mm, with $x_2 = 0$ and $x_3 = 25.8$ mm.

Some of the striking features of these and other space-time Green's functions are the singularities they contain. These are called wave arrivals and are associated with points on the slowness surface where $\mathbf{s}.\mathbf{x}$ is stationary. These wave arrival singularities propagate outwards from the source at the group velocities in each direction, and thus lie on the wave surface, i.e., the locus of ray vectors scaled by a factor $t$. Figure 2.4 shows the zonal section of the L and qT sheets of the wave surface of zinc [37] (the pure T sheet is not shown since these T waves are SH polarized and are not coupled to in $G_{33}$). The qT sheet is folded, giving rise to multiple wave arrivals near the [001] direction.

The analytical form of a wave arrival singularity is ascertained by approximating the equation of the slowness surface with a polynomial function in the region around the stationary phase point, and then integrating analytically [37, 48]. What emerges is that, for convex and concave regions of the slowness surface ($L_1$, $L_2$ both negative or both positive), $G_{ij}(\mathbf{x}, t)$ displays a discontinuity of magnitude proportional to $\Lambda/x\sqrt{|K|}$, together with a change in slope. The arrivals L and S are of this form, with the response being zero before the longitudinal arrival L and constant after the last shear arrival S. For saddle-shaped regions of the slowness surface ($L_1$, $L_2$ opposite in sign), $G_{ij}(\mathbf{x}, t)$ displays a logarithmic divergence, an example of which is the arrival I. Along the zonal axis of transversely isotropic solids such as zinc, for which the slowness surface is concave in the region of the zonal axis, there is a conical point in the ray surface, and this gives rise to the negative square root singularity of the arrival X, which is associated with the phenomenon of external conical refraction [61]. These wave arrivals correspond to intersections of the viewing direction with sheets of the wave surface of zinc as shown in Figure 2.4.

### 2.4.2 Half-Space Response

The sorts of experiments that measure the response functions of solids, more often than not, involve forces being applied and measurements being carried out at surfaces. One might expect, therefore, that half-space Green's

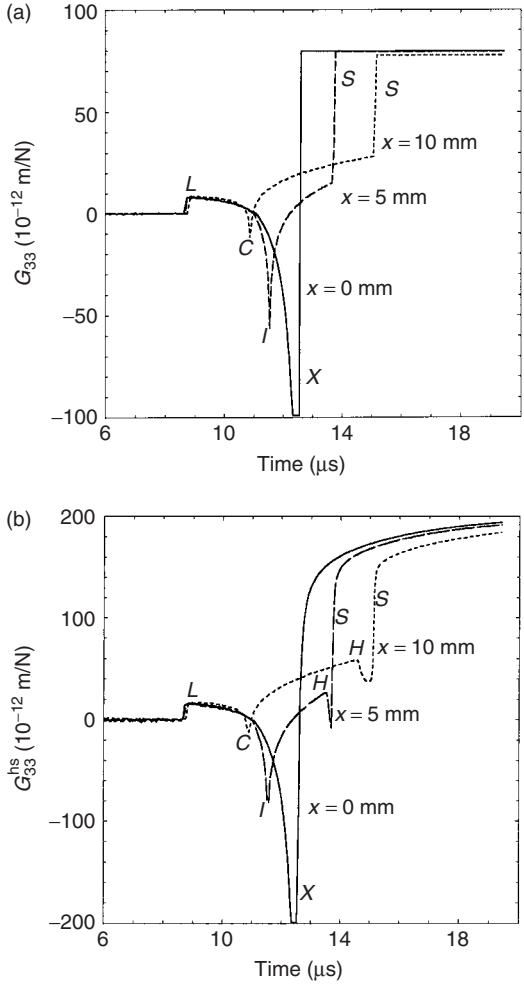


FIG. 2.3. (a) Calculated infinite continuum response function $G_{33}(\mathbf{x}, t)$ for hexagonal zinc, for three observation points $x_1 = 0$ mm, 5 mm, and 10 mm, with $x_2 = 0$ and $x_3 = 25.8$ mm. (b) Corresponding half-space Green's functions $G_{33}^{hs}(\mathbf{x}, t)$. The elastic constants are from [60].

functions or the Green's functions for a layer would more accurately model the results of these experiments. Calculation of the half-space Green's function for an interior point requires evaluation of the two-dimensional integral in Eq. 2.13. In the case of a generally anisotropic solid, this can be done entirely numerically [39] or, using the Cagniard-de Hoop method, to evaluate

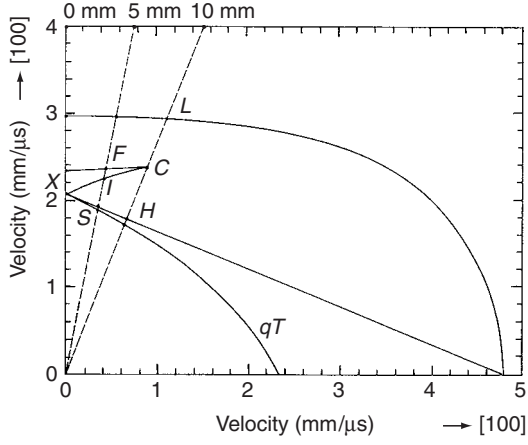


FIG. 2.4. Zonal section of the L and qT sheets of the wave surface of zinc.

one of the integrals analytically [40, 41]. The results obtained by the two approaches are identical. Figure 2.3(b) shows the calculated zinc half-space response functions $G_{ss}^{hs}(\mathbf{x}, t)$ for the same configurations as in Figure 2.3(a). Overall, the displacements are greater in magnitude by about a factor of 2 as compared with those for the infinite continuum, as one might expect. The bulk wave arrivals have the same analytic form and occur at the same times as for the half-space calculation, and for early times and near epicentral directions, the two response functions are almost indistinguishable. After the last T wave arrival, while the infinite continuum response $G_{33}(\mathbf{x}, t)$ is constant, the half-space response $G_{33}^{hs}(\mathbf{x}, t)$ approaches asymptotically a constant value. This last-mentioned feature is a diffraction effect originating at the surface.

For observation points well away from epicenter, where the surfaces of the sample play an increasingly important role, the two responses are no longer so similar. For the half-space an additional wavefront appears, called the head wave [62]. This is the sharp downward kink marked H in Figure 2.3(b) and the wave surface similarly labeled in Figure 2.4. A head wave can be thought of as being made up of a family of slower (transverse) waves trailing the faster (longitudinal) wave as it skims along the surface, much like in the formation of a supersonic cone. Zinc is somewhat unusual in that the head wave merges with the qT sheet of the wave surface at a point very close to the conical point [62]. These calculated responses are in very good agreement with waveforms measured in zinc by Kim *et al.* [63, 64], particularly with regard to the bulk and head wave arrivals.

Along the surface of the solid there is also the Rayleigh wavefront, which lags behind the slowest T wavefront, and which along the surface propagates

the dominant singularity. This is discussed in Section 2.5. For a thick plate, there are also numerous multipass wave arrivals, encompassing the various possible mode conversion sequences. The generalized ray approximation [47, 65] is a starting point for calculations of the complete waveform for a thick plate of arbitrary anisotropy, but to date there has not been much in the way of numerical implementation of this method for modeling experiment. The main difficulty is keeping track of the large number of poles that occur. In the case of viscoelastic solids, these poles lie off the real axis, and numerical integration becomes a viable option for computing the response of an anisotropic plate [35, 66]. The complex issue of poles is sidestepped in finite difference calculations (see, e.g., [67]).

### 2.4.3 Inversion of Capillary Fracture Waveform Data

A method of simulating a concentrated normal force on the surface of a sample with a step function time dependence is to place a thin glass capillary on the surface and press the sharp edge of a razor blade down on it until it breaks [5, 6]. At this instant the approximate point load on the surface drops abruptly to zero. The waveform that is generated is of large amplitude and can be accurately monitored with a small-aperture capacitive transducer placed elsewhere on the surface of the sample. This method has been applied to a variety of solids.

A complete waveform contains a great deal of information that can be used to recover elastic constants. Every and Kim [23] have determined elastic constants of silicon from individual capillary fracture-generated waveforms obtained on a (001)-oriented Si single crystal, confining their attention to near epicentral measurements and data extending only as far as the last T wave arrival, and interpreting this information on the basis of the infinite continuum Green's function, which is adequate in this region, where the HW does not exist.

Figure 2.5 shows a measured epicentral waveform for silicon and the outcome of a simple optimization process based on a succession of grid searches in which the elastic constants $C_{12}$ and $C_{44}$ have been determined by fitting the calculated infinite continuum Green's function to the measured waveform. The fit is close, and the values of $C_{12}$ and $C_{44}$ obtained are in good agreement with accepted values, 63GPa and 79.1GPa, respectively [60]. The position of the dip followed by the steep rise is most sensitive to the value of $C_{44}$, and the depth of the dip is mainly controlled by $C_{12}$. Interestingly, from phase velocity measurements in the (001) direction of a cubic crystal, it is not possible to obtain the value of $C_{12}$.

### 2.4.4 Observation of Wave Arrivals

In some experiments, it is only the singularities in a waveform, where most of the acoustic energy is concentrated, that can be clearly distinguished, the

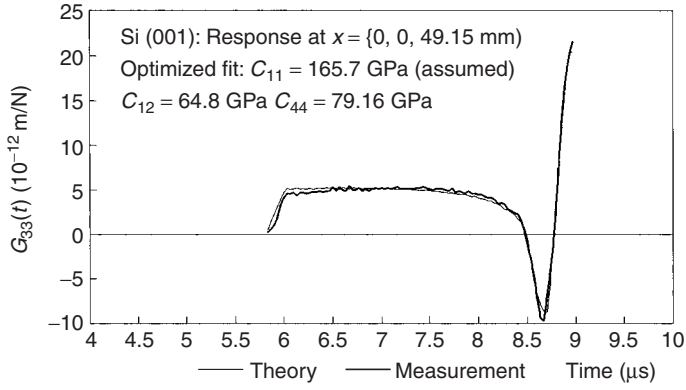


FIG. 2.5. Measured and calculated epicentral waveforms for Si(001).

remaining features being obscured by transducer ringing and other experimental artifacts. This is particularly true of laser ultrasound measurements [8–10]. A number of groups have consequently devoted their efforts to measuring wave arrivals, reconstructing part of the wave surface, and then working backwards to determine the elastic constants.

2.4.4.1 Laser Ultrasound Measurements. In recent years laser ultrasound measurements have been carried out on a number of anisotropic solids, including silicon and zinc single crystals and a variety of fiber composites [1, 68] (for a review, see Castagnede and Berthelot [69]). In the standard approach, as depicted in Figure 2.6(a), a focused Q-switched laser delivers a heat pulse to a small region on the surface of a specimen, causing a transient acoustic wave to be launched into the specimen. The wavefield is measured on the opposite face using interferometry or a small-aperture piezoelectric or capacitive transducer, which senses the normal displacement of the surface. Note that it is the thermally generated sound wave that is detected, not the thermal phonons making up the heat pulse as in phonon imaging. At low power densities the thermoacoustic generation mechanism predominates. The sudden rise in temperature of the surface brings about a localized radial stress field within the surface, and this results in acoustic radiation. At higher power densities, material is ablated from the surface, and this gives rise to an impulsive reaction force normal to the surface. The generation and detection processes are both axisymmetric in form, and only waves with a significant sagittal component to their polarizations feature in the observations.

Figure 2.6(b) shows typical waveforms obtained by Every *et al.* [1] on a 10-mm-thick (001)-oriented silicon single crystal with detection at epicenter and at 8 mm from epicenter. Although the wave arrivals are recognizable from the signal onsets, little information can be inferred directly from these

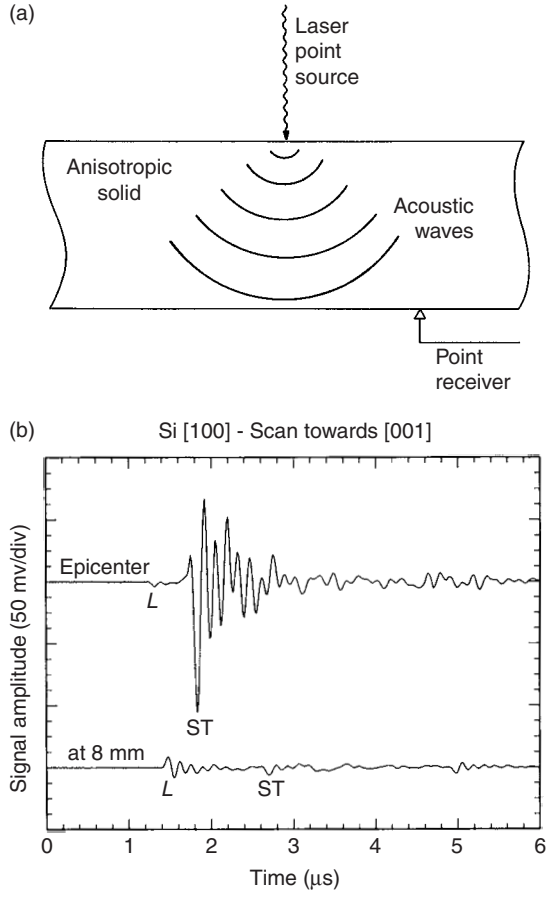


FIG. 2.6. (a) Schematic of a laser ultrasound experiment. (b) Laser ultrasound waveforms measured in a (001)-oriented Si crystal with a small-aperture piezoelectric transducer.

signals concerning the continuous portions of the waveforms in between the singularities.

Figure 2.7(a) shows a scan image obtained by stacking together a large number of waveforms for a closely spaced set of excitation points, and representing the resulting $(x, t)$ response as a gray-scale image [1]. Figure 2.7(b) shows the theoretical wave arrivals obtained by a Monte Carlo procedure that assumes a uniform distribution of wave normals $\mathbf{n}$, and then plots as points the arrival times of those rays that come within the detector aperture for each value of $x$. The calculated scan image features the first L and ST

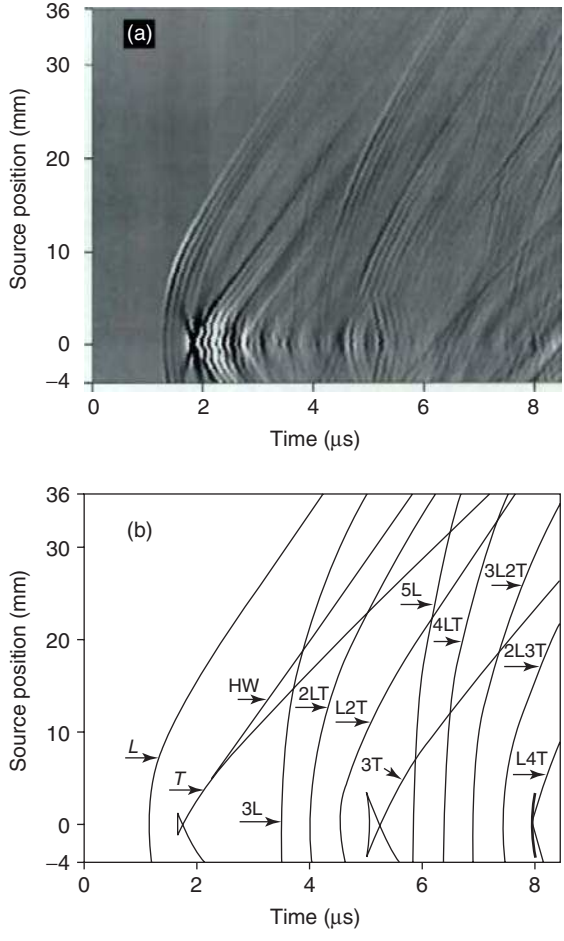


FIG. 2.7. (a) Scan image for a (001)-oriented 10-mm-thick Si crystal, generated from a closely spaced set of excitation points in the [100] direction. (b) Calculated scan image.

wave arrivals, the head wave (HW), and the arrivals of various mode conversion sequences for passage of the wavefield three and five times through the sample. The multipass and head waves are calculated using standard procedures for dealing with reflection in anisotropic solids [52]. These various wave arrivals are all in good agreement with the signal onsets in the measured scan image. There is no discernable presence of FT single- or multipass waves, or any mode conversion sequence or head wave involving FT waves. This is because the FT waves are almost perfectly shear-horizontally (SH) polarized,

and are therefore uncoupled from the axisymmetric mode of excitation and detection. The single- and multipass wave arrivals and head wave are all in good agreement with experiment. Castagnede *et al*. [70] have carried out a similar study on fiber composites using the Cagniard-de Hoop method to do the simulations.

In viscoelastic solids there is rounding of the wave arrivals due to dispersion. Guilbaud and Audoin [35] have used wavelet analysis to process waveforms measured on polymer matrix composites, thereby obtaining more accurate (frequency-dependent) wave arrival times. Another device for obtaining more accurate wave arrivals, used by Audoin *et al*. [71], is to locate peaks in the radiation power, calculated from the measured signal and its Hilbert transform.

### 2.4.5 Inversion to Obtain Elastic Constants from Group Velocity Data

The inverse problem of obtaining elastic constants from group velocity data is, in general, more complicated than for phase velocity data. The main reason is that, in cubic or lower-symmetry materials, the group velocity for a particular nonsymmetry direction cannot be obtained by analytic means; it needs to be computed numerically. One method of doing so is to choose a starting value of the wave normal $\mathbf{n}$, calculate the phase velocity $v(\mathbf{n})$ by diagonalizing the Christoffel tensor, obtain the group velocity $\mathbf{V}$ by one of the methods described in Section 2.3.1, and then adjust $\mathbf{n}$ until $\mathbf{V}$ points in the required direction. Building on this procedure, Every and Sachse [24] have implemented the following double iterative strategy for recovering elastic constants $C_{\alpha\beta}$ from a set of measured group velocities. With a starting set of $C_{\alpha\beta}$'s, $\mathbf{V}$'s having the directions but not in general the magnitudes of the measured $\mathbf{V}$'s are obtained. A succession of steadily improving values of the $C_{\alpha\beta}$'s are then generated, which at each step reduce the mean square difference between the measured and calculated $\mathbf{V}$'s.

Table 2.2 shows the elastic constants of Si that Every and Sachse [24] have obtained from laser ultrasound measurements. They are in good agreement with tabulated values. This algorithm has been used on a number of materials, including composites with different ply-layup configurations [72, 32]. Figure 2.8 shows group velocity data measured in a cross-ply graphite–epoxy

TABLE 2.2. Elastic Constants of Si

| | $C_{11}(GPa)$ | $C_{12}(GPa)$ | $C_{44}(GPa)$ |
|---|---|---|---|
| Every and Sachse [24] | 165.1 | 65.0 | 80.2 |
| Tabulated values [60] | 165 | 63 | 79.1 |

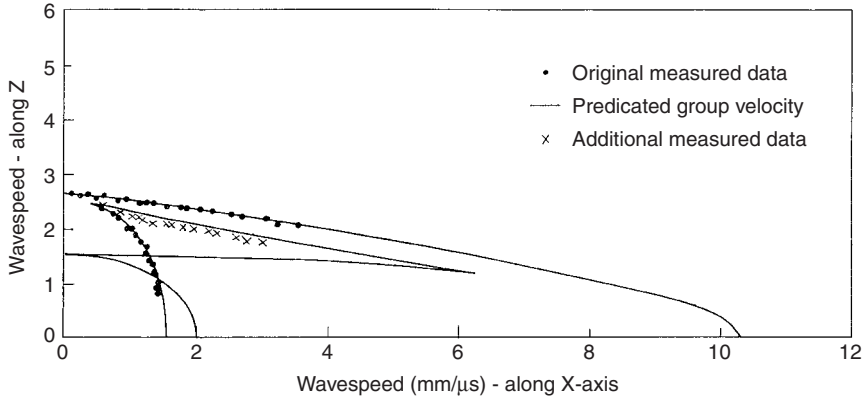


FIG. 2.8. Group velocity data measured in a cross-ply graphite–epoxy specimen by Niu [72].

specimen by Lin Niu [72], using capillary fracture generation and capacitive detection, together with her fitted group velocity curve. Her recovered values of the elastic constants are $C_{11} = C_{22} = 185$, $C_{33} = 12.0$, $C_{44} = C_{55} = 4.14$, and $C_{13} = C_{23} = 3.96$ GPa. A number of other authors have subsequently implemented similar schemes. Minachi *et al.* [73] have determined elastic constants of a number of unidirectional graphite–epoxy composite plates from the group velocities of longitudinal pulses that are generated at one surface of the sample, reflected from the opposite surface, and then detected elsewhere at the first surface using piezoelectric transducers. Their material is transversely isotropic, which simplifies the calculations a bit since the plane in which the wave normal lies is known.

In directions where the wave surface is folded, the algorithm described previously for determining the wave normals can become unstable because of the multiplicity of wave arrivals in these directions. An alternative approach, based on the Cagniard-de Hoop method, has been developed by Deschamps and Bescond [74], and is claimed to be more robust. It has been implemented on laser-generated data to obtain the elastic constants of silicon [71]. A pitfall that has to be carefully negotiated when using data from near cuspidal edges of the wave surface is that a sharp feature persists in the waveform well beyond the cuspidal edge [20, 37, 71], and it is difficult to distinguish this from an actual wave arrival.

In laser ultrasound, the first L arrival tends to be the clearest and most accurately measurable, with later arrivals being partially obscured by their proximity and by noise. Although it is tempting, therefore, to try to base an elastic constant determination on L data alone, Every and Sachse [75] and

Castagnede *et al.* [76] have shown that longitudinal velocities depend most sensitively on the partial set of elastic constants $C_{11}$, $C_{22}$, $C_{33}$, $(C_{12} + 2C_{66})$, $(C_{23} + 2C_{44})$, and $(C_{13} + 2C_{55})$, and it is only these constants that can be accurately recovered from longitudinal velocity data.

2.4.5.1 Symmetry Plane Measurements. For minimization of experimental error, it is recommended and indeed is quite a common practice in crystallography to determine the elastic constants from wave speeds measured in symmetry planes that contain symmetry axes. For media of orthorhombic or higher symmetry, the diagonal elements $C_{\alpha\alpha}, \alpha = 1, 2, \ldots 6$ are determined from measured speeds of longitudinal and transverse waves propagating in symmetry directions, since variations of these wave speeds with deviation of their wave normals from the symmetry direction are zero to first order. Along the principal axes, group and phase velocities coincide and the elastic constant $C_{\alpha\alpha}$ is given simply by $\rho v^2$ for the relevant velocity. Determination of the mixed-index elastic constants $C_{\alpha\beta}, \alpha \neq \beta$, is carried out using measurements of the group velocities of quasi-longitudinal and quasi-transverse modes propagating along oblique directions in symmetry planes, for which directions of corresponding wave normals are found from an analytic equation expressed in terms of elastic constants that include both pure- and mixed-index elastic constants. The mixed-index elastic constants are then calculated from a closed-form analytic formula that relates them to the magnitude of the group velocity, its direction and corresponding wave normal. It is also noted that pure-index shear moduli, such as $C_{44}$, $C_{55}$, and $C_{66}$, can also be determined from measurements of group velocities of a shear-horizontally (SH) polarized pure transverse mode propagating along oblique directions in symmetry planes. Kim *et al.* [29–31] developed this procedure and determined the elastic constants of cubic silicon, hexagonal zinc, and an orthorhombic PEEK (poly ether ether ketone) composite from group velocities measured in symmetry planes of these materials.

For data pertaining to certain high-symmetry directions such as fourfold axes in cubic and tetragonal media, the sixfold axis in hexagonal media, and twofold axes in orthorhombic media, around which a transverse slowness sheet is concave-shaped, it is possible to derive closed-form expressions relating the group velocities to the $C_{\alpha\beta}$'s, not only for the modes whose **n**'s lie in the symmetry direction, but also for the so-called oblique modes whose **n**'s lie away from the axis in symmetry planes. These expressions allow the $C_{\alpha\beta}$'s to be obtained by analytic means [77, 78]. Litian Wang [79] has carried out a general analysis of this problem using Stroh's formalism. The inversion is simplest for wave arrivals whose normals lie in the symmetry directions, because in that case phase and group velocities coincide. Kim *et al.* [80] have obtained elastic constants of Si from multipass arrivals by this means. Aussel

and Monchalin [22], who were pioneers in the use of laser-generated ultrasound for elastic constant determination, also focused on measurements in symmetry directions.

## 2.5 Surface Response

When detection is carried out on the same surface as excitation, the response is dominated by Rayleigh surface acoustic waves (SAW) or pseudo-SAW (pSAW). The feature labeled RW represents the slowness curve of the SAW in the (001) surface of copper. It is the slowest propagating wave arrival and hence appears latest in the surface displacement signal. The family of SAW rays emanating from the point of excitation is normal to this curve. There are two regions in that diagram where the slowness curve is concave, whereas elsewhere it is convex. As a result, the SAW group velocity curve is folded in a complicated way near the ⟨100⟩ directions as shown in the inset in Figure 2.9(a), and the surface response to point excitation exhibits multiple SAW arrivals, as seen for the calculated response for the [100] direction, represented by the solid curve in Figure 2.9(a) [81]. The cuspidal points where the folding occurs correspond to points of inflection (zero curvature) in the RW slowness curves. In much the same way as for bulk phonon focusing, this is accompanied by intense focusing of SAW energy flux. SAW focusing has been extensively studied, both theoretically and experimentally, by Maznev and coworkers [82], and could provide a means for determining elastic constant ratios.

In and near the [110] direction, we see that the response is dominated by a pSAW, which lies within the band of bulk wave excitations. The calculated point force response for the [110] direction is shown by the chain dotted curve in Figure 2.9(a). Essentially identical results are obtained using the Cagniard-de Hoop technique [41]. The deep dip in this curve is the pSAW arrival, and the displacement continues to increase after this until the end of the bulk wave continuum.

In addition to the SAW arrivals, there are bulk L, FT, and ST wave arrivals that appear at earlier times in the surface response (points a, b, and c in Figure 2.9(a)). These are much less pronounced than the SAW arrivals.

Figure 2.9(b) shows the corresponding measured responses of the (001) surface of a Cu single crystal obtained by capillary fracture excitation and capacitive detection [81]. Apart from experimental rounding in the measured signals, the measured and calculated responses are in good agreement. Fitting calculated to measured surface responses is thus a way of obtaining the elastic constants of solids, whether the full waveform data are used or only the wave arrivals.

Chai and Wu [25], relying only on SAW arrivals, have measured the directional dependence of the group velocities of point focus laser-generated SAW

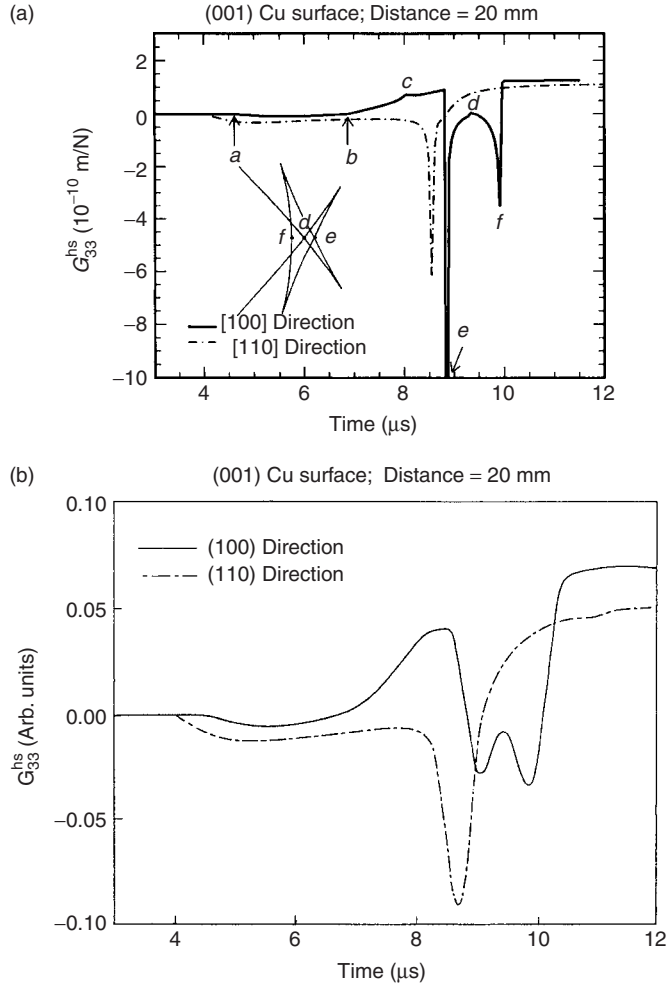


FIG. 2.9. (a) Calculated and (b) measured surface response of a (001)-oriented copper crystal in the [100] and [110] directions.

in the (111) surface of silicon and in a unidirectional fiber composite, and have used a simplex optimization method to recover the elastic constants of this solid. Their algorithm is similar to the one described earlier in this chapter for bulk waves. With starting values of $C_{\alpha\beta}$, they calculate a set of group velocities that point in the observation directions and thereby obtain the mean square difference $\chi^2$ between calculated and measured velocities. The $C_{\alpha\beta}$ are then varied to progressively improve the fit and minimize $\chi^2$.

It is usually the case, except for highly anisotropic materials, that the SAW velocity is more sensitive to the shear moduli than longitudinal moduli such as $C_{11}$. It is therefore advantageous for the purpose of elastic constant determination if bulk longitudinal wave arrivals can also be measured in one or more directions. This approach has been effectively applied by Wu *et al.* [83] to determine the elastic constants of concrete using transient waves excited by ball impact and the use of a conical transducer.

## 2.6 Plate Modes

We consider here the response of a thin anisotropic plate to pointlike excitation by laser or other means. The characteristic wavelengths radiated are supposedly much greater than the thickness $h$ of the plate, i.e., $kh \ll 1$, and so we are concerned only with the three lowest plate modes:

(1) The flexural or antisymmetric mode $A_0$. This mode is dispersive, with the absolute value of slowness being proportional to $\omega^{-1/2}$. Taking the $z$-direction normal to the plate, and the $x$- and $y$-directions in the plate, the directional dependence of the slowness $\mathbf{s}$ of this mode is given by [84, 85]

$$\gamma_{11}s_x^4 + 4\gamma_{16}s_x^3 s_y + 2(\gamma_{12} + 2\gamma_{66})s_x^2 s_y^2 + 4\gamma_{26}s_x s_y^3 + \gamma_{22}s_y^4 = \frac{12\rho}{\omega^2 h^2} \tag{2.23}$$

(2) Two coupled horizontally polarized modes satisfying [84–86]

$$\begin{pmatrix} \Gamma_{11} - 1 & \Gamma_{12} \\ \Gamma_{21} & \Gamma_{22} - 1 \end{pmatrix} \begin{pmatrix} u_x \\ u_y \end{pmatrix} = 0 \tag{2.24}$$

$$\Gamma_{11} = (\gamma_{11}s_x^2 + 2\gamma_{16}s_x s_y + \gamma_{66}s_y^2)/\rho$$

$$\Gamma_{12} = \Gamma_{21} = (\gamma_{16}s_x^2 + (\gamma_{12} + \gamma_{66})s_x s_y + \gamma_{26}s_y^2)/\rho$$

$$\Gamma_{22} = (\gamma_{66}s_x^2 + 2\gamma_{26}s_x s_y + \gamma_{22}s_y^2)/\rho$$

The coefficients $\gamma_{ij}$ are the stiffnesses appropriate to plane stress, and are functions of the elastic constants $C_{ij}$. For the practically important case of $(x, y)$ being a symmetry plane of an orthotropic medium, $\gamma_{ij} = (C_{ij} - C_{i3}C_{j3}/C_{33})$ for $i, j = 1, 2$; $\gamma_{66} = C_{66}$, and $\gamma_{16} = \gamma_{26} = 0$. In the isotropic limit the last two modes are uncoupled and become the lowest symmetric Lamb mode $S_0$ and the lowest shear horizontal mode $SH_0$.

Plate modes exhibit focusing, much as for SAW, with the focusing intensity being inversely proportional to the curvature of the slowness curve. In the case of the flexural mode and the slower of the two coupled modes, the slowness

curve can have concave regions, and consequently there can be focusing caustics. The characteristic patterns of these caustics for cubic symmetry materials have been worked out by Maznev and Every [85].

Measurements of the laser-generated dispersive flexural mode response of a silicon wafer have been carried out by Nakano and Nagai [87]. Chen and Man [88] have carried out measurements on the slower $SH_0$-like mode in an anisotropic cold-rolled aluminium sheet.

Veidt and Sachse [33] have carried out an extensive study of the coupled plate modes in a Si wafer and in unidirectional graphite–epoxy laminates, using a pulsed laser beam as a dipole source and a small-aperture piezoceramic transducer as a monopolar source, as well as a piezoceramic sensor that responds to lateral and shear motion of the specimen surface. By these means they were able to generate scan images for the plate modes. They have modeled the wave arrivals with calculated plate mode group velocities. For the fiber composites, accurate fits were obtained both outside and within the cuspidal regions of the wave surface. Consistent values were obtained for the stiffness coefficients $\gamma_{11}$, $\gamma_{22}$, $\gamma_{12}$, and $C_{66}$.

## 2.7 Conclusions

The PS/PR approach to measuring the elastic properties of solids is now well established, and has proved of value in a number of applications. The advantages of PS/PR techniques are manifold and varied. Wave propagation over a wide range of directions can be studied and many elastic constants recovered in an experiment on a single specimen, obviating the need for accurate cutting and faceting of samples. Laser excitation and interferometric detection permit noncontact measurement of elastic constants. Elastic properties can be inferred from measurements carried out on one side of a specimen, which has obvious applications in the nondestructive inspection of structures for materials' degradation. PS/PR techniques exist for studying large specimens as well as small specimens, thin plates, and so on.

PS/PR techniques span the time domain (transient excitation) as well as the frequency domain (tone burst excitation), and in essence measure the time or frequency domain Green's function of a solid. The theoretical modeling that is required for extracting information about a specimen from measured data is generally much more complicated than for plane wave techniques, but easily within the capability of any modern personal computer. Measurements carried out in the far field, which encompasses phonon imaging, the measurement of wave arrivals by laser techniques, etc., can be interpreted on the basis of the ray approximation, which is a significant simplification. In the special case of data pertaining to symmetry directions, for which the phase and group

velocities coincide, the elastic constant recovery is the same as for plane wave techniques.

There remain many challenging problems both from an experimental point of view and in modeling and interpretation, but PS/PR techniques are sufficiently well established that one can anticipate their continued use in a wide variety of applications.

## References


1. Every, A.G., and Sachse, W. (1991). *Phys. Rev*. **B44**: 6689; Every, A.G., Sachse, W., Kim, K.Y., and Thompson, M.O. (1990). *Phys. Rev. Lett*. **65**: 1446.
2. Wolfe, J.P. (1998). *Imaging of Phonons*, Cambridge: Cambridge University Press.
3. Maris, H.J. (1971). *J. Acoust. Soc. Am*. **50**: 812; Maris, H.J. (1986). In *Nonequilibrium Phonons in Nonmetallic Crystals*, Eisenmenger, W., and Kaplyanskii, A.A., eds., Amsterdam: North Holland.
4. Aki, K., and Richards, P. (1980). *Quantitative Seismology*, San Francisco: Freeman.
5. Breckenridge, F.R., Tschiegg, C.E., and Greenspan, M. (1975). *J. Acoust. Soc. Am*. **57**: 626.
6. Kim, K.Y., Niu, L., Castagnede, B., and Sachse, W. (1989). *Rev. Sci. Instrum*. **60**: 2785.
7. Hsu, N.N. (May, 1976). U.S. Patent 4,018,084.
8. Bunkin, F.V., Kolomenskii, A.A., and Mikhalevich, V.G. (1991). *Lasers in Acoustics* Chur: Harwood.
9. Hutchings, D.A. (1988). In *Physical Acoustics*, p. 21, vol. 18, Mason, W.P., and Thurston, R.N., eds., New York: Academic.
10. Scruby, C.B., Dewhurst, R.J., Hutchings, D.A., and Palmer, S.B. (1982). In *Research Techniques in Nondestructive Testing*, p. 281, vol. V, Sharpe, R.S., ed., New York: Academic.
11. Cargill, G.S. (1981). *Physics Today* **34**(10): 27.
12. Kim, K.Y., and Sachse, W. (1983). *Appl. Phys. Lett*. **43**, 1099.
13. Monchalin, J.P., Heron, R., and Muzak, N. (1985). *Rev. Sci. Instrum*. **56**: 543.
14. Dewhurst, R.J., Edwards, C., McKie, A.D.W., and Palmer, S.B, (1988). *J. Appl. Phys*. **63**: 1225.
15. Calder, C.A., Draney, E.C., and Wilcox, W.W. (1981). *J. Nucl. Mater*. **27**: 126.
16. Briggs, A. (1992). *Acoustic Microscopy*, Oxford: Clarendon.
17. Every, A.G., and Briggs, G.A.D. (1998). *Phys. Rev*. **B58**: 1601.
18. Hauser, M.R., Weaver, R.L., and Wolfe, J.P. (1992). *Phys. Rev. Lett*. **68**: 2604; Weaver, R.L., Hauser, M.R., and Wolfe, J.P. *Z. Phys*. **B90**: 27.
19. Wesner, J., Wurz, K.U., Hillmann, K., and Grill, W. (1993). In *Phonon Scattering in Condensed Matter*, vol. VII, Meissner, M., and Pohl, R.O. eds., Berlin: Springer-Verlag.
20. Kim, K.Y., Bretz, K.C., Every, A.G., and Sachse, W. (1996). *J. Appl. Phys*. **79**: 1857.
21. Sachse, W. (1987). *Ultrasonics International '87 Conference Proceedings*, p. 419, Guildford: Butterworth.
22. Aussel, J.D., and Monchalin, J.P. (1989). *Ultrasonics* **27**: 165.
23. Every, A.G., and Kim, K.Y. (1996). *Ultrasonics* **34**: 471.
24. Every, A.G., and Sachse, W. (1990). *Phys. Rev*. **B42**: 8196.

25. Chai, J.F., and Wu, T.T. (1994). *J. Acoust. Soc. Am*. **95**: 3232.
26. Audoin, B., Bescond, C., and Deschamps, M. (1996). *J. Appl. Phys*. **80**: 3760.
27. Wuerz, K.U., Wesner, J., Hillmann, K., and Grill, W. (1995). *Z. Phys*. **B97**: 487.
28. Grill, W., Hillmann, K., Wuerz, K.U., and Wesner, J. (1996). In *Advances in Acoustic Microscopy*, p. 167. vol. 2, Briggs, A., and Arnold, W., eds., New York: Plenum.
29. Kim, K.Y., Sribar, R., and Sachse, W. (1995). *J. Appl. Phys*. **77**: 5589.
30. Kim, K.Y. (1994). *Phys. Rev*. **B49**: 3713.
31. Kim, K.Y., Ohtani, T., Baker, A.R., and Sachse, W. (1995). *Res. Nondestr. Eval*. **7**: 13.
32. Sachse, W., Every, A.G., and Grabec, I. (1991). In *Enhancing Analysis Techniques for Composite Materials*, p. 77, NDE-Vol. 10, Schwer, L., Reddy, J.N., and Mal, A., eds., New York: ASME-AMD.
33. Veidt, M. and Sachse, W. (1994). *J. Acoust. Soc. Am*. **96**: 2318.
34. Sachse, W., Shiwa, M., Kishi, T., and Thompson, M.O. (1994). In *Nondestructive Characterization of Materials VI*, p. 291, Green, R.E., and Ruud, C.O., eds., New York: Plenum.
35. Guilbaud, S., and Audoin, B. (1999). *J. Acoust. Soc. Am*. **105**: 2226.
36. Kim, K.Y., Every, A.G., and Sachse, W. (1994). *J. Acoust. Soc. Am*. **95**: 1942.
37. Every, A.G., and Kim, K.Y. (1994). *J. Acoust. Soc. Am*. **95**: 2505.
38. Wang, C.-Y., and Achenbach, J.D. (1993). *Wave Motion* **18**: 273; (1995). *Proc. Roy. Soc. Lond*. **A449**: 441.
39. Every, A.G., Kim, K.Y., and Maznev, A.A. (1997). *J. Acoust. Soc. Am*. **102**: 1346; Maznev, A.A., and Every, A.G. (1997) *Int. J. Eng. Sci*. **35**: 321.
40. Mourad, A., and Deschamps, M. (1995). *J. Acoust. Soc. Am*. **97**: 3194.
41. Bescond, C., and Deschamps, M. (1998). *J. Acoust. Soc. Am*. **103**: 114.
42. Wang, C.-Y., and Achenbach, J.D. (1996). *Wave Motion* **24**: 227.
43. Buchwald, V.T. (1959). *Proc. R. Soc. Lond*. **A253**: 563.
44. Burridge, R. (1967). *Q. J. Mech. Appl. Math*. **20**: 42.
45. Duff, G.F.D. (1960). *Phil. Trans. Roy. Soc*. **252**: 249.
46. Tewary, V.K., and Fortunko, C.M. (1992). *J. Acoust. Soc. Am*. **91**: 1888.
47. Van der Hijden, J.H.M.T. (1987). *Propagation of Transient Elastic Waves in Stratified Anisotropic Media*, Amsterdam: North Holland.
48. Payton, R.G. (1983). *Elastic Wave Propagation in Transversely Isotropic Media*, The Hague: Martinus Nijhoff.
49. Yeats, F.R. (1984). *Phys. Rev*. **B29**: 1674.
50. Auld, B.A. (1990). *Acoustic Fields and Waves in Solids*, Malabar: Krieger.
51. Fedorov, F.I. (1968). *Theory of Elastic Waves in Crystals*, New York: Plenum.
52. Musgrave, M.J.P. (1970). *Crystal Acoustics*, San Francisco: Holden-Day.
53. Every, A.G., Koos, G.L., and Wolfe, J.P. (1984). *Phys. Rev*. **B29**: 2190.
54. Maris, H.J. (1971). *J. Acoust. Soc. Am*. **50**: 812.
55. Northrop, G.A., and Wolfe, J.P. (1980). *Phys. Rev*. **B22**: 6196.
56. Every, A.G. (1981). *Phys. Rev*. **B24**: 3456.
57. Metzger, W., and Huebener, R.P. (1988). *Z. Phys*. **B73**: 33.
58. Maris, H.J. (1983). *Phys. Rev*. **B28**: 7033.
59. Berry, M.V. (1976). *Adv. Phys*. **25**: 1.
60. Every, A.G., and McCurdy, A.K. (1992). *Landolt Bornstein, Numerical Data and Functional Relationships in Science and Technology*, vol. 29a, Berlin: Springer.
61. Kim, K.Y., Sachse, W., and Every, A.G. (1993). *Phys. Rev. Lett*. **70**: 3443; (1994). *Int. J. Mod. Phys*. **B8**: 2327.
62. Musgrave, M.J.P., and Payton, R.G. (1981). *Q. J. Mech. Appl. Math*. **34**: 235.

63. Kim, K.Y., and Sachse, W. (1994). *J. Appl. Phys*. **75**: 1435.
64. Kim, K.Y. (1994). *Wave Motion* **20**: 83.
65. Pao, Y.H., and Gajewski, R.R. (1977). In *Physical Acoustics*, p. 183, vol. 13, Mason, W.P., and Thurston, R.N., eds., New York: Academic; Pao, Y.-H., Gajewski, R.R., and Ceranoglu, A.N. (1978) *J. Acoust. Soc. Am*. **65**: 96.
66. Weaver, R.L., Sachse, W., and Kim, K.Y. (1996). *J. Appl. Mech*. **63**: 338; Weaver, R.L., Sachse, W., and Niu, L. (1989). *J. Acoust. Soc. Am*. **85**: 2255.
67. Chang, C., and Sun, C.T. (1988). *Composites Science and Technology* **33**: 213.
68. Sachse, W., Every, A.G., and Thompson, M.O. (1990). *Am. Soc. Mech. Eng*. AMD-Vol. **116**: 51.
69. Castagnede, B., and Berthelot, Y. (1992). *J. d'Acoustique* **5**: 417.
70. Castagnede, B., Deschamps, M., Mottay, E., and Mourad, A. (1994). *Acta Acustica* **2**: 83.
71. Audoin, B., Bescond, C., and Deschamps, M. (1996). *J. Appl. Phys*. **80**: 3760.
72. Niu, L. (1992). PhD Dissertation, Cornell University, Ithaca, New York.
73. Minachi, A., Hsu, D.K., and Thompson, R.B. (1994). *J. Acoust. Soc. Am*. **96**: 353.
74. Deschamps, M., and Bescond, C. (1995). *Ultrasonics* **33**: 205.
75. Every, A.G., and Sachse, W. (1992). *Ultrasonics* **30**: 43.
76. Castagnede, B., Every, A.G., and Sachse, W. (1992). *C.R. Acad. Sci. Paris*, t. **314**, Serie II: 865.
77. Kim, K.Y., and Sachse, W. (1993). *Phys. Rev*. **47**: 10993.
78. Kim, K.Y., Every, A.G., and Sachse, W. (1996). *Int. J. Mod. Phys*. **B10**: 235.
79. Wang, L. (1995). *J. Phys. Condens. Mat*. **7**: 3863.
80. Kim, K.Y., Sachse, W., and Every, A.G. (1993). *J. Acoust. Soc. Am*. **93**: 1393.
81. Every, A.G., Kim, K.Y., and Maznev, A.A. (1998). *Ultrasonics* **36**: 349.
82. Kolomenskii, A.A., and Maznev, A.A. (1993). *Phys. Rev*. **B48**: 14502; (1991). *JETP Lett*. **53**: 423; Maznev, A.A., and Every, A.G., *Solid State Commun*. **97**: 679.
83. Wu, T.T., Fang, J.S., Liu, G.Y., and Kuo, M.K. (1995). *J. Acoust. Soc. Am*. **98**: 2142; Wu, T.T., and Fang, J.S. (1997). *J. Acoust. Soc. Am*. **101**: 330.
84. Lekhnitskii, S.G., Tsai, S.W., and Cheron, T. (1968). *Anisotropic Plates*, New York: Gordon and Breach.
85. Maznev, A.A., and Every, A.G. (1995). *Acta Acustica* **3**: 387.
86. Wu, T.T., and Chiu, S.T. (1992). *Ultrasonics* **30**: 60.
87. Nakano, H., and Nagai, S. (1991). *Ultrasonics* **29**: 230.
88. Chen, H.Y., and Man, C.S. (1994). In *Rev. Prog. in QNDE*, p. 149, vol. 13A, Thompson, D.O., and Chimenti, D.E., eds., New York: Plenum.